# First-Principles and Numerical Investigation of a High-Efficiency Lead-Free Rb₂NaGaBr₆-Based Perovskite Solar Cell

**Md. Jahidul Islam[1]*and Mahbub Alam Rabin[2]**

[1]Department of Materials and Metallurgical Engineering, Dhaka University of Engineering & Technology, Gazipur, Bangladesh
[2]Department of Materials and Metallurgical Engineering Bangladesh University of Engineering and Technology, Bangladesh

## ABSTRACT

Lead-free double perovskites have emerged as promising alternatives to conventional lead-based perovskite solar cells (PSCs), offering improved environmental safety and long-term stability. In this study, we explore the photovoltaic potential of a novel, non-toxic double perovskite material, Rb₂NaGaBr₆, using a Density Functional Theory and utilize it to design and simulate a new PCS by using SCAPS-1D simulation approach. DFT analysis reveals a direct bandgap of 1.56 eV, low effective carrier masses, and higher carrier mobility, indicating excellent optoelectronic properties. Based on these DFT explored properties, a planar solar cell architecture—Glass/FTO/TiO₂/Rb₂NaGaBr₆/Cu₂O/Au was modeled and simulated in SCAPS-1D. The device showed favorable energy band alignment and charge extraction characteristics. Upon optimizing the thicknesses and absorption layer defect density, the structure achieved a power conversion efficiency (PCE) of 27.004%, with Voc = 1.274 V, Jsc = 25.20 mA/cm², and FF = 88.08%. These findings establish Rb₂NaGaBr₆ as a viable and efficient candidate for next-generation lead-free photovoltaic technologies.

## 1. INTRODUCTION

In recent years, the global energy sector has experienced an increased emphasis on sustainable and renewable energy sources. Among these, solar energy stands out due to its abundant availability and potential to meet the world's energy demands. It has been reported that the sun provides over 1500 exawatt-hours of energy annually, which is more than 200 times the total energy reserve of all fossil fuels combined [1]. Harnessing 0.3% of this energy could significantly reduce reliance on non-renewable resources and lower the environmental footprint of power generation [1]. Traditional solar cells, including silicon-based or gallium arsenide (GaAs) technologies, have achieved considerable efficiency over the years. However, their production involves complex processes, high costs, and in some cases, the use of scarce or toxic materials [2]. To address these limitations, researchers have shifted their focus toward alternative photovoltaic (PV) technologies. Among them, PSCs have emerged as a transformative solution due to their excellent optoelectronic properties and low-cost fabrication potential. These attributes have driven significant progress in PSCs, which have rapidly evolved from an initial 3.8% efficiency to over 26% in single-junction cells and 34% in perovskite-silicon tandem configurations [3][4][5]. This rapid development is largely attributed to the favorable properties of halide perovskite materials, such as high absorption coefficient, long charge carrier diffusion lengths, low exciton binding energy, and tunable bandgap. Different lead-based perovskites like MAPbI₃ have a PCE of 22.4% [6], CsPbI₃ with a PCE of 21.15% [7], FAMAPbI₃ with a PCE of 23.32 % [8] show excellent efficiency. However, most of the high-performing perovskites contain lead (Pb), which poses significant environmental and health hazards. Lead is known to be highly toxic and water-soluble, making its leakage from solar panels a serious concern for both ecosystems and human safety [9].

In the pursuit of sustainable and non-toxic alternatives to lead-based perovskites, researchers have increasingly turned their attention to a new class of materials known as lead-free double perovskites. These compounds, typically represented by the general formula A₂M⁺M³⁺X₆, replace lead with a combination of monovalent and trivalent cations, offering a promising pathway toward safer and more stable solar cell technologies. Among them, materials such as Cs₂AgBiI₆ have already demonstrated encouraging results, achieving PCE of up to 21.59% while maintaining thermal and chemical stability [10].

---

*Corresponding author's email: jahidulislam@duet.ac.bd

Others, like $Cs_2AgGaBr_6$, have shown even greater theoretical promise, with simulated PCEs reaching as high as 32.57% under optimized conditions [11]. Yet, despite these advances, the search continues for a material that not only delivers high efficiency but also leverages abundant, non-toxic elements. It is within this context that we explore $Rb_2NaGaBr_6$, a relatively unstudied double perovskite composed of rubidium ($Rb^+$), sodium ($Na^+$), gallium ($Ga^{3+}$), and bromine ($Br^-$). Each of these elements is earth-abundant and environmentally benign, making $Rb_2NaGaBr_6$ a strong candidate for future green photovoltaic technologies. Beyond the absorber layer itself, the performance of a perovskite solar cell also hinges on the materials used to transport charge carriers. The electron transport material (ETM) and hole transport material (HTM) play a crucial role in guiding the photogenerated electrons and holes toward their respective electrodes with minimal resistance and recombination. To serve as an effective window layer, the ETM must be an n-type semiconductor with a wide bandgap, allowing most incident light to reach the absorber beneath it. These layers work in tandem with the perovskite to ensure that the flow of charge is as smooth and efficient as possible, forming the backbone of a high-performing solar cell. It is important to note that a recent study investigated a structurally similar perovskite, $Rb_2LiInBr_6$, using DFT and SCAPS-1D simulations, and achieved a notable PCE of 26.90% with $TiO_2$ and $Cu_2O$ as transport layers, optimizing both defect density and absorber thickness to reach a configuration with $Voc = 1.277$ V, $Jsc = 25.06$ mA/cm², and FF = 83.96% [12]. While that work validated the photovoltaic viability of Rb-based double perovskites, the material chemistry and transport layer strategy differed from ours.

Our research utilizes Density Functional Theory (DFT) to explore the electronic structure, bandgap, electron affinity, relative dielectric constant and carrier mobility of $Rb_2NaGaBr_6$. The DFT analysis reveals that the material has a direct bandgap of approximately 1.56 eV, which lies within the optimal range for single-junction solar cells. To evaluate the photovoltaic performance, we employed SCAPS-1D simulations using a typical layered architecture: $FTO/TiO_2/Rb_2NaGaBr_6/Cu_2O/Au$. The selection of $TiO_2$ as the ETM is based on its high transparency, wide bandgap, and good electron mobility [1]. $Cu_2O$ is chosen as the HTM due to its suitable energy band alignment and strong hole conductivity.

Furthermore, the impact of absorber layer thickness and bulk defect concentration was systematically analyzed to identify the optimal conditions for peak device performance. The simulations revealed that an absorber thickness of 800 nm delivers the most favorable outcome. Under this configuration, the solar cell achieved a maximum PCE of 27.004%, accompanied by a short-circuit current density (Jsc) of 25.20 mA/cm², an open-circuit voltage (Voc) of 1.274 V, and a fill factor (FF) of 84.08%. These findings are consistent with prior studies, where optimizing layer thickness significantly enhanced the device output [5], [6]. The growing interest in lead-free and stable perovskite materials necessitate the discovery of new candidates that can offer better performance without compromising on safety. $Rb_2NaGaBr_6$ shows promise as a sustainable and efficient light absorber in next-generation solar cells. This study contributes to the ongoing efforts to develop viable alternatives to lead-based perovskites by presenting simulation-backed evidence of high efficiency and stable performance in a carefully designed device structure. In summary, this work introduces $Rb_2NaGaBr_6$ as a potential material for efficient and environmentally friendly perovskite solar cells. Through a combination of DFT-based electronic structure calculations and SCAPS-1D numerical simulations, we demonstrate its applicability and advantages in a practical solar cell configuration. The insights gained from this study may guide future experimental efforts in the development and fabrication of high-performance, lead-free perovskite photovoltaics.

## 2. METHODOLOGY

This research integrates first-principles quantum mechanical modeling and device-level numerical simulation to evaluate the suitability and performance of a novel lead-free double perovskite material, $Rb_2NaGaBr_6$, for photovoltaic applications. The investigation involves optoelectronic calculations using DFT and solar cell modeling using SCAPS-1D.

### 2.1 Device Structure

Fig. 1 illustrates the schematic structure of the proposed planar solar cell, comprising the following layered configuration: $Glass/FTO/TiO_2/Rb_2NaGaBr_6/Cu_2O/Au$. The glass substrate serves as the mechanical support for the entire device. Fluorine-doped tin oxide (FTO) functions as a transparent conducting front electrode, allowing incident light to reach the active layer while simultaneously acting as the negative contact for electron collection. Titanium dioxide ($TiO_2$), with its wide bandgap and high electron mobility, serves as the electron transport layer (ETL) and extracts photo-generated electrons from the absorber layer. The active layer, $Rb_2NaGaBr_6$, is a newly explored,

non-toxic double perovskite material with a theoretically predicted direct bandgap of approximately 1.56 eV. This absorber is expected to provide strong visible light absorption and efficient charge carrier transport. Cuprous oxide (Cu₂O) is used as the hole transport layer (HTL) due to its excellent hole mobility, favorable valence band alignment, and chemical stability. Gold (Au) is selected as the back electrode, providing an efficient interface for hole collection and ensuring high conductivity. Fig.2. illustrates the energy band alignment of the proposed photovoltaic system.

## 2.2  First-Principles DFT Simulation

First-principles calculations based on DFT were performed using the Vienna Ab Initio Simulation Package (VASP). The Projector Augmented-Wave (PAW) method was employed to represent the interaction between the valence electrons and the ionic cores. Exchange-correlation energy was treated within the Generalized Gradient Approximation (GGA), utilizing the revised Perdew–Burke–Ernzerhof (PBEsol) functional, which is specifically optimized for solid-state systems.
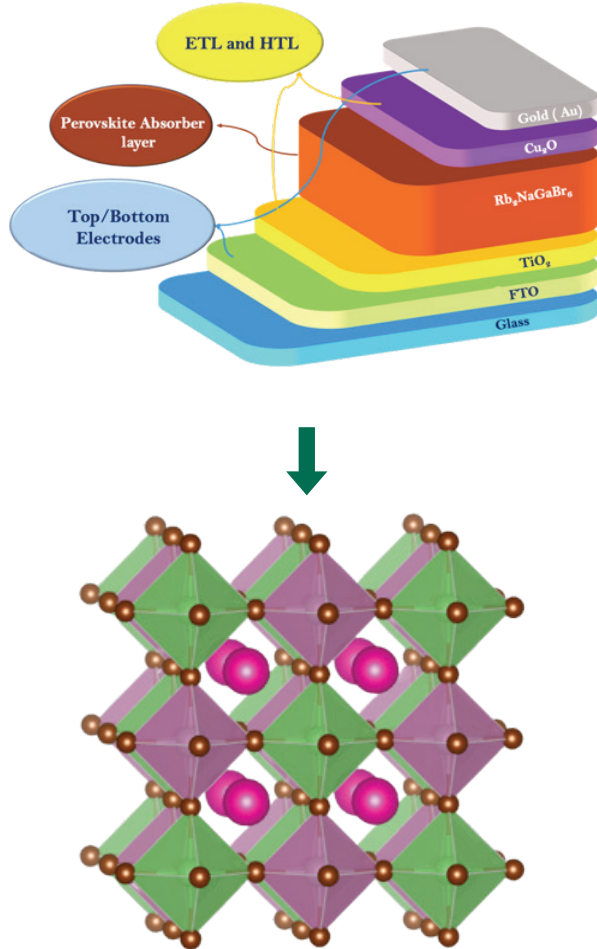


**Fig. 1:** Structural Architecture of the Proposed Device

The calculations were carried out using a plane-wave energy cutoff of 520 eV. A Monkhorst–Pack k-point mesh of 9×9×9 was used for structural relaxation, which was refined to 11×11×11 for the calculation of the electronic band structure and density of states. Geometry optimization was considered converged when the total energy difference between successive steps was less than $10^{-8}$ eV and the residual forces on each atom were less than 0.001 eV/Å. In this study, the electronic band structure of Rb₂NaGaBr₆ was calculated using the GGA within the PBEsol functional. A line-mode band structure calculation was carried out by sampling the electronic eigenvalues along the standard high-symmetry directions in the first Brillouin zone, specifically following the path Γ → X → W → K → Γ → L. To ensure sufficient resolution of the dispersion features, 30 k-points were interpolated between each pair of high-symmetry points.
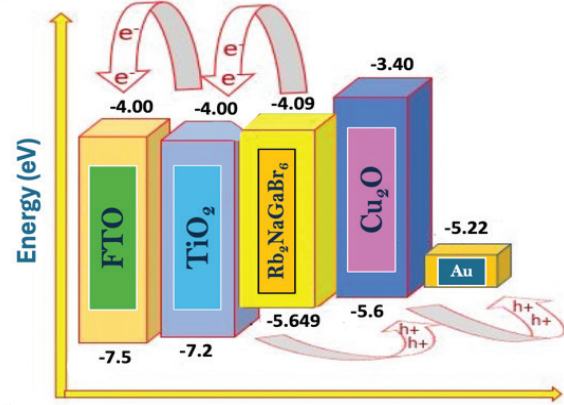


**Fig. 2:** Energy Band Alignment of the Proposed Device

The effective masses of charge carriers were calculated by performing second-order polynomial fitting to the energy–momentum (E–k) dispersion near the conduction band minimum (CBM) and valence band maximum (VBM), using the expression:

$$m^* = \hbar^2 \left( \frac{d^2E}{dk^2} \right)^{-1} \qquad (1)$$

The carrier mobility was estimated from the effective mass using the relaxation time approximation as follows:

$$\mu = \frac{e\tau}{m^*} \qquad (2)$$

Where, $\tau$ is the scattering time, assumed to be $2\times10^{-14}$ s for semiconductors [13]. Additionally, the effective density of states for the conduction and valence bands were calculated using the relations:

$$N_C = 2 \left( \frac{2\pi m_e^* K_B T}{h^2} \right)^{3/2} \qquad (3)$$

$$N_v = 2 \left( \frac{2\pi m_h^* K_B T}{h^2} \right)^{3/2} \qquad (4)$$

The extracted parameters, such as bandgap, effective masses, mobilities, effective density of states and dielectric permittivity, were incorporated into the SCAPS-1D simulation environment to assess device-level performance.

## 2.3 Numerical Simulation Using SCAPS-1D

The SCAPS-1D software, developed at the University of Gent, was used to simulate the performance of the full solar cell structure. The program solves the fundamental set of equations governing the operation of a semiconductor device, which include Poisson's equation and the continuity equations for electrons and holes under steady-state illumination conditions. Poisson's equation is expressed as:

$$\frac{d}{dx}\left( \varepsilon \frac{d\phi}{dx} \right) = -q\left(p - n + N_D^+ - N_A^-\right) \qquad (5)$$

The electron and hole continuity equations are:

$$\frac{dn}{dt} = \frac{1}{q}\frac{dJ_n}{dx} + G_n - R_n \qquad (6)$$

$$\frac{dp}{dt} = -\frac{1}{q}\frac{dJ_p}{dx} + G_p - R_p \qquad (7)$$

Here, is the electrostatic potential, $\varepsilon$ is the dielectric permittivity, q is the elementary charge, n and p are the electron and hole concentrations, are the current densities, and G and R represent generation and recombination rates, respectively. Shockley–Read–Hall recombination was used to model trap-assisted recombination in the absorber.

Table I presents the key physical and electronic parameters of each layer in the Glass/FTO/TiO$_2$/Rb$_2$NaGaBr$_6$/Cu$_2$O/Au device structure. These values, obtained from DFT calculations and validated literature were used in SCAPS-1D to simulate charge transport, recombination and band alignment behavior.

The simulations were conducted under standard AM 1.5G illumination with an incident power of 1000 W/m$^2$ and at a temperature of 300 K. The thicknesses of the FTO and metal contact layers were set based on experimentally common values, while the absorber layer thickness was varied between 200 nm and 1300 nm. Similarly, the bulk defect density in the absorber was varied over the range of $10^8$ to $10^{19}$ cm$^{-3}$ to evaluate its impact on photovoltaic parameters such as Voc, Jsc, FF, and PCE.

**Table I:** Material Parameters Used in SCAPS-1D Simulation

| Parameters | FTO [14] | TiO$_2$ [15] | Rb$_2$NaGaBr$_6$ | Cu$_2$O [15] |
|---|---|---|---|---|
| $W$ (nm) | 50 | 100 | 80 | 200 |
| $E_G$ (eV) | 3.5 | 3.2 | 1.559 | 2.17 |
| $X$ (eV) | 4.00 | 4.20 | 4.09 | 3.20 |
| $\varepsilon$R | 9.00 | 9.00 | 10.21 | 7.11 |
| $N_C$ (cm$^{-3}$) | $2.2 \times 10^{18}$ | $1.0 \times 10^{19}$ | $1.768 \times 10^{18}$ | $2.02 \times 10^{19}$ |
| $N_V$ (cm$^{-3}$) | $1.8 \times 10^{19}$ | $1.0 \times 10^{19}$ | $5.104 \times 10^{18}$ | $1.1 \times 10^{19}$ |
| $V_{TE}$ (cm/s) | $1 \times 10^7$ | $1 \times 10^7$ | $1 \times 10^7$ | $1 \times 10^7$ |
| $V_{TP}$ (cm/s) | $1 \times 10^7$ | $1 \times 10^7$ | $1 \times 10^7$ | $1 \times 10^7$ |
| $\mu_n$ (cm$^2$/Vs) | 20 | 20 | 100 | 200 |
| $\mu_p$ (cm$^2$/Vs) | 10 | 10 | 45 | 80 |
| $N_D$ (cm$^{-3}$) | $2 \times 10^{19}$ | $2 \times 10^{19}$ | $2 \times 10^{19}$ | 0 |
| $N_A$ (cm$^{-3}$) | $1 \times 10^{15}$ | 0 | $1 \times 10^{19}$ | $2 \times 10^{19}$ |
| $N_T$ (cm$^{-3}$) | $1 \times 10^{15}$ | $1 \times 10^{15}$ | $1 \times 10^{13}$ | $1 \times 10^{14}$ |

## 3. RESULTS AND DISCUSSION

### 3.1 ETL Layer Optimization

To evaluate the impact of ETL thickness on the photovoltaic performance of the proposed solar cell, a systematic simulation was conducted by varying the thickness of the TiO$_2$ (ETL) in the range of 0.025 μm to 0.3 μm, in increments of 0.025 μm. During this analysis, the thicknesses of the absorber (Rb$_2$NaGaBr$_6$) and the HTL (Cu$_2$O) were kept constant at 0.3 μm and 0.2 μm, respectively, to isolate the effect of the ETL. Key photovoltaic parameters—namely Voc, Jsc, FF, and PCE—were extracted for each configuration.

The simulation results reveal that variations in the TiO$_2$ layer thickness exert a minimal influence on the overall device performance. Specifically, the PCE and FF remain nearly unchanged across the examined range, shown in Fig. 3, indicating that carrier extraction from the conduction band of the absorber to the ETL is not significantly hindered by thinner ETL layers. This is likely due to TiO$_2$'s high electron mobility and wide bandgap, which ensure efficient electron transport even at reduced thicknesses. As a result, a minimal ETL thickness of 0.03 μm was found sufficient to maintain high performance while also benefiting from material and cost savings in practical implementations. Therefore, this value is selected as the optimal ETL thickness for the proposed device configuration.
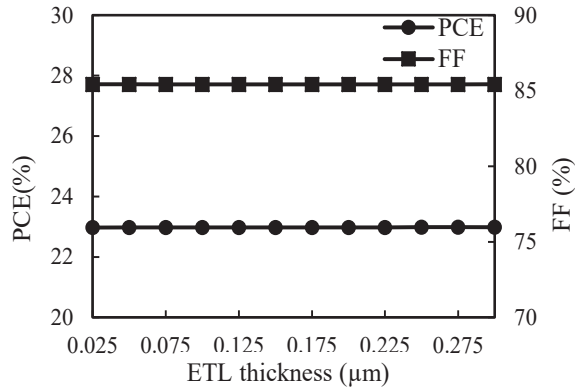
**Fig. 3:** Effect of ETL Layer Thickness on Power Conversion Efficiency and Fill Factor



**Fig. 5:** Effect of HTL Layer Thickness on Short Circuit Current and Open Circuit Voltage

### 3.2 HTL Layer Optimization

Following ETL optimization, the effect of hole transport layer thickness on device performance was investigated using a similar parametric approach. The thickness of the Cu$_2$O (HTL) was varied from 0.025 μm to 0.3 μm, while maintaining constant thicknesses of the ETL (0.03 μm) and the absorber (0.3 μm). The goal was to determine the optimal Cu$_2$O thickness that maximizes carrier extraction and minimizes energy losses at the absorber/HTL interface. Fig. 4 and Fig. 5 show that unlike the ETL, the Cu$_2$O HTL displayed a noticeable influence on photovoltaic performance. An increase in HTL thickness led to a gradual improvement in both PCE and Jsc, while the FF remained relatively stable. The Voc showed little variation, indicating that the increase in efficiency is primarily driven by enhanced current generation rather than changes in the built-in potential. This enhancement can be attributed to the favorable band alignment of Cu$_2$O with Rb$_2$NaGaBr$_6$ and its high hole mobility, which allows for effective collection of photo-generated holes. Moreover, Cu$_2$O's absorption onset in the visible range facilitates the transmission of high-energy photons to the absorber, further boosting carrier generation.
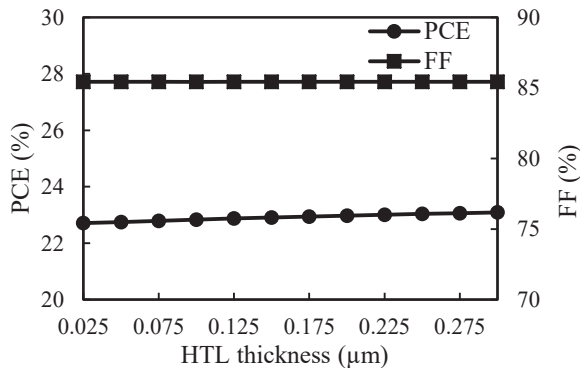


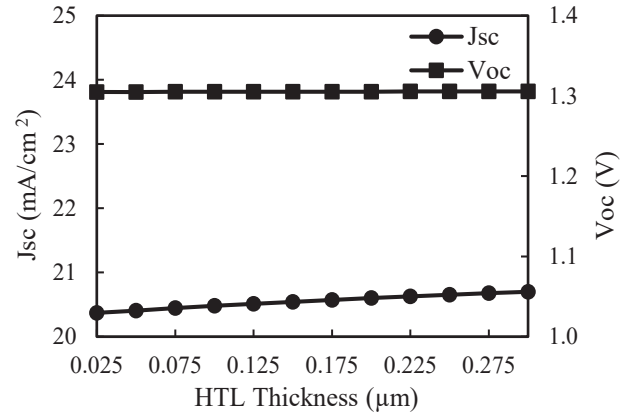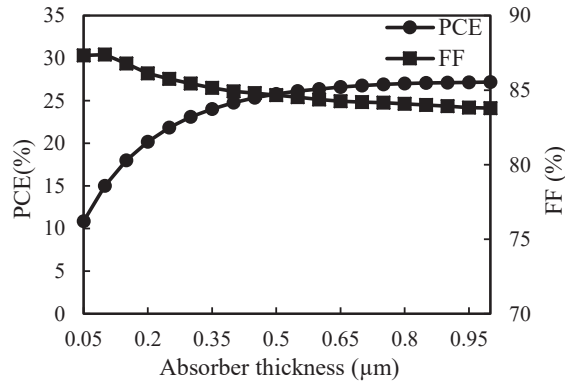**Fig. 4:** Effect of HTL Layer Thickness on Power Conversion Efficiency and Fill Factor

From the observed trend, it is evident that a thicker Cu$_2$O layer enables more efficient hole extraction and reduces recombination losses at the interface. Consequently, a thickness of 0.3 μm was determined as the optimum value for the HTL, balancing carrier transport, optical transparency, and material usage. This selection contributes to the overall high efficiency of the device and underlines the importance of precise interface engineering in lead-free perovskite solar cells.

### 3.3 The Effect of Absorber Layer Thickness on Photovoltaic Performance

The thickness of the absorber layer is a key determinant of a solar cell's overall efficiency, as it directly governs light absorption, carrier generation, and transport dynamics. Following the optimization of the ETL and HTL thicknesses, the absorber layer thickness was systematically varied to evaluate its influence on the photovoltaic performance of the Rb$_2$NaGaBr$_6$-based device. Simulations were carried out by increasing the thickness of the absorber from 0.05 μm to 1.0 μm in increments of 0.05 μm, while maintaining constant thicknesses for the ETL and HTL layers at 0.03 μm and 0.3 μm, respectively. The results reveal that an increase in absorber thickness leads to a sharp and nearly exponential rise in the J$_{sc}$, shown in Fig. 7, driven by the enhanced absorption of incident photons and the generation of a larger number of electron–hole pairs. This enhancement, however, begins to saturate beyond a certain thickness as optical absorption nears its upper limit. The simulations indicate that J$_{sc}$ begins to plateau around 0.8 μm, marking a point of diminishing returns with further thickness increase.

In contrast, the $V_{oc}$ exhibits a gradual decline with increasing absorber thickness. This is attributed to enhanced bulk recombination, which becomes more prominent in thicker layers due to longer carrier transit paths and limited diffusion lengths. The effect of absorber layer on PCE and FF is shown in Fig. 6, and it is found that when the absorber thickness exceeds the effective carrier diffusion length, recombination losses dominate, leading to a decline in Voc and, in turn, affecting the FF and PCE.



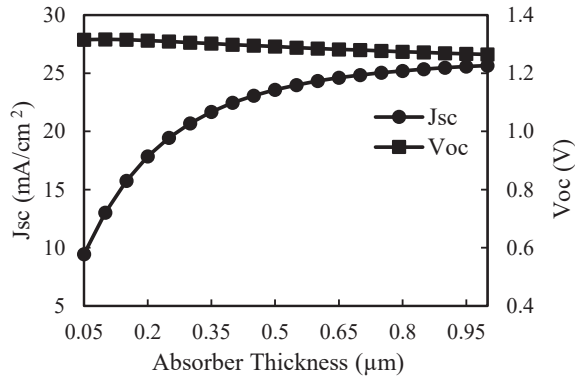**Fig. 6:** Effect of Absorber Layer Thickness on Power Conversion Efficiency and Fill Factor



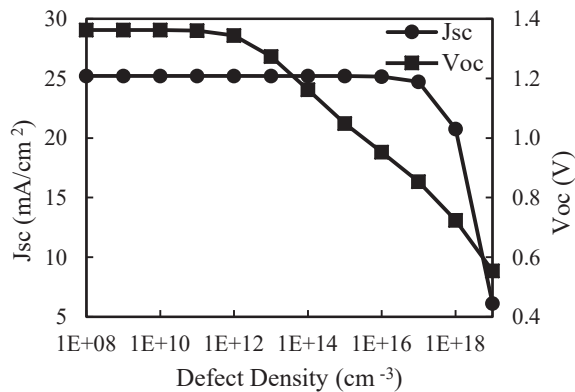**Fig. 7:** Effect of Absorber Layer Thickness on Short Circuit Current and Open Circuit Voltage



**Fig. 8:** Effect of Bulk Defect Density on Power Conversion Efficiency and Fill Factor

The trade-off between $J_{sc}$ enhancement and $V_{oc}$ degradation highlights the importance of identifying an optimal absorber thickness that maximizes overall efficiency. In this study, a thickness of 0.8 μm was found to provide the best compromise, leading to a peak PCE of 27.08%. This value corresponds to the point where photon absorption is near-saturated, while recombination losses remain adequately controlled. These findings reinforce the critical role of absorber layer optimization in the performance tuning of lead-free perovskite solar cells.

### 3.4 Effect of Bulk Defect Density of the Absorber Layer on PV Performance

Bulk defect density plays a critical role in determining the recombination dynamics within the absorber layer, and consequently, the overall performance of a solar cell. These defects—introduced during material processing—can act as non-radiative recombination centers by trapping charge carriers, reducing their lifetime, and increasing Shockley–Read–Hall (SRH) recombination. To assess this effect, the defect density of the Rb₂NaGaBr₆ absorber layer was varied from $1 \times 10^8$ to $1 \times 10^{19}$ cm⁻³ while keeping other parameters constant. The effect of bulk defect density on PCE and FF is shown in Fig. 8 and on short circuit current and open circuit voltage is expressed in Fig. 9.
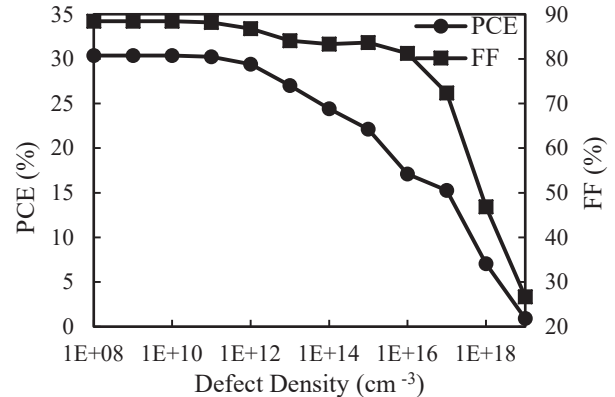


**Fig. 9:** Effect of Bulk Defect Density on Short Circuit Current and Open Circuit Voltage

Simulation results reveal that device performance remains largely unaffected for defect densities up to $1 \times 10^{12}$ cm⁻³, with minimal changes in $V_{oc}$ and $J_{sc}$. However, beyond this threshold, particularly between $1 \times 10^{13}$ and $1 \times 10^{16}$ cm⁻³, performance metrics begin to decline. This decline becomes exponential at higher defect levels due to reduced carrier diffusion length and increased recombination losses. The most severe degradation is observed at a defect density of $1 \times 10^{19}$ cm⁻³, where the PCE drops to a minimum of 0.905%. The FF follows

a similar trend, initially declining gradually and then dropping sharply beyond $1 \times 10^{16}\,cm^{-3}$. Based on these observations, an optimized defect density of $1 \times 10^{13}\,cm^{-3}$ is selected for modeling, as it offers a balance between material tolerances and device performance. This result emphasizes the necessity of precise fabrication control to limit defect formation and ensure reliable high-efficiency operation of lead-free perovskite solar cells.

### 3.5 Effect of Working Temperature on PV Performance

Temperature is a vital environmental factor affecting the operational stability and efficiency of photovoltaic devices. Thermal variations can alter charge carrier mobility, layer interfaces, and bandgap energy, leading to either performance enhancement or degradation depending on the thermal stability of the materials involved. To study this effect, the $Rb_2NaGaBr_6$-based solar cell was simulated across a temperature range of 275 K to 450 K, in increments of 25 K, under standard illumination conditions. Fig. 10 reveals the effect of this on PCE and FF and Fig. 11 reveals the effect on Jsc and Voc. Fig. 10 shows that at the baseline temperature of 275 K, the device exhibits its highest efficiency of 28.1%, along with a fill factor of 85.62%. As the temperature increases, both PCE and FF gradually decline, reaching 20.6% and 76.04%, respectively, at 450 K. This decline is attributed to increased phonon scattering and enhanced non-radiative recombination, which negatively impact carrier lifetimes and reduce charge collection efficiency. Interestingly, the PCE remains above 20.6% throughout the temperature range, suggesting that the device maintains functional stability even at elevated temperatures.
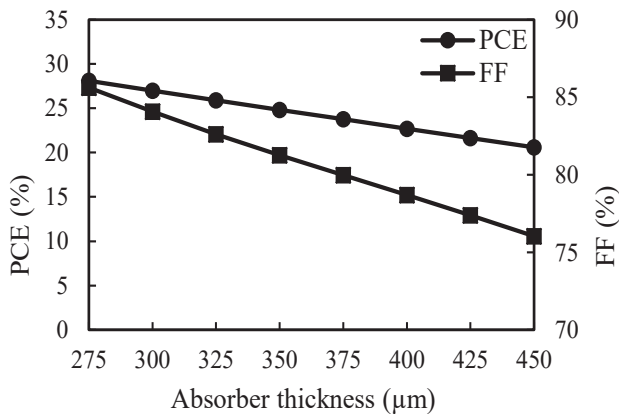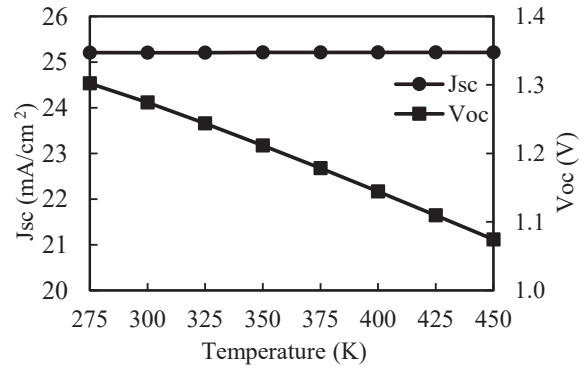


**Fig. 11:** Effect of Temperature on Short Circuit Current and Open Circuit Voltage

$V_{oc}$ shows a clear inverse correlation with temperature, steadily decreasing as thermal energy disturbs the built-in potential and widens the recombination window. In contrast, Jsc remains relatively stable across the range, with only minor fluctuations. These results indicate that while thermal management is crucial for maximizing output, the proposed $Rb_2NaGaBr_6$ device architecture retains robust photovoltaic characteristics under varying environmental conditions, reinforcing its applicability for real-world deployment.

### 3.6 Benchmarking SCAPS-1D Results with Previously Reported Data

Table II presents a comparative analysis of the photovoltaic performance of various previously reported devices alongside our proposed structure. The designed configuration-—FTO/TiO₂/Rb₂NaGaBr₆/Cu₂O/Au—demonstrates a remarkable power conversion efficiency of 27.004%, highlighting a strong synergy between open-circuit voltage and short-circuit current density. This performance significantly surpasses that of other reported double perovskite-based PSCs, underscoring the superior potential of our device architecture.



**Fig. 10:** Effect of Temperature on Power Conversion Efficiency and Fill Factor

**Table II:** Comparison of PV Parameters of Perovskite Structures with Previously Reported Data.

| Device Structure | Voc (V) | Jsc (mA/cn | FF (%) | PCE (%) |
|---|---|---|---|---|
| FTO/SnO₂/Rb₂NaGaBr₆ CuI/W [16] | 1.278 | 25.02 | 84.01 | 26.86 |
| FTO/TiO₂/Rb₂LiInBr₆ Cu₂O/Ni [17] | 1.277 | 25.06 | 83.96 | 26.90 |
| ITO/ZnO₂/Cs₂BiAgI₆ CBTS/Au [18] | 1.09 | 23.76 | 83.78 | 21.59 |
| ITO/WS₂/Cs₂CuBiBr₆ CBTS/Ni [19] | 0.712 | 35.63 | 77.57 | 19.70 |
| FTO/TiO₂/Rb₂NaGaBr₆ Cu₂O/Au [This work] | 1.274 | 25.20 | 88.08 | 27.004 |

## 4. CONCLUSION

This work presents a detailed theoretical and numerical analysis of the photovoltaic potential of $Rb_2NaGaBr_6$, a novel lead-free double perovskite material. Through DFT calculations, the material was shown to possess a direct bandgap and favorable carrier transport properties, making it suitable for solar energy harvesting. The electronic parameters extracted from the DFT simulation were used to model a solar cell device in SCAPS-1D, featuring a layered structure of $FTO/TiO_2/Rb_2NaGaBr_6/Cu_2O/Au$. The device demonstrated outstanding performance under optimized simulation conditions, achieving a power conversion efficiency of 27.004%. The influence of absorber layer thickness and bulk defect density was also investigated, confirming the material's tolerance to minor structural variations. Additionally, energy band alignment analysis showed efficient charge separation and minimal recombination losses due to appropriate ETL and HTL selection. Overall, the results suggest that $Rb_2NaGaBr_6$ is a viable candidate for stable, efficient, and environmentally friendly perovskite solar cells and warrants further experimental validation for real-world deployment.

## REFERENCES

[1] W. A. Herrmann, "Quantifying global energy resources," Energy, Vol. 31, No. 12, pp. 1685–1702, 2006.

[2] R. E. H. Sims, H. Rogner and K. Gregory, "Carbon emission and mitigation cost comparisons between fossil fuel, nuclear and renewable energy resources for electricity generation," Energy Policy, Vol. 31, No. 13, pp. 1315–1326, 2003.

[3] M. A. Green, E. D. Dunlop, J. Hohl-Ebinger, M. Yoshita and A. W. Y. Ho-Baillie, "Solar cell efficiency tables (Version 64)," Prog. Photovolt. Res. Appl., Vol. 32, No. 7, pp. 425–441, 2024.

[4] W. S. Yang, B. W. Jung, N. J. Jeon, D. U. Lee, S. S. Shin, J. Kim, K. E. Kim, H. S. Jeong and S. I. Seok, "Iodide management in formamidinium-lead halide-based perovskite layers for efficient solar cells," Science, Vol. 356, No. 6345, pp. 1376–1379, 2017.

[5] Z. Li, B. Wu, X. Sheppard, S. Zhang, S. Gao, D. Long, N. Zhu and J. Zhu, "Organometallic-functionalized interfaces for highly efficient inverted perovskite solar cells," Science, Vol. 376, No. 6591, pp. 416–420, 2022.

[6] J. Wang, Z. Li, J. Li, S. Wei, and S. Suhaily, "α-CsPbI₃ perovskite solar cells fabricated via an efficient two-step process," Mater. Today, Vol. 55, No. 12, pp. 2103–2109, 2023.

[7] W. Guo et al., "Low-temperature flexible MAPbI₃ perovskite solar cells," Chem. Eng. J., Vol. 448, Art. No. 142366, 2023.

[8] Q. Jiang et al., "Surface passivation of perovskite film for efficient solar cells," Nat. Photonics, Vol. 13, No. 7, pp. 460–466, 2019.

[9] V. Srivastava, R. K. Chauhan, and P. Lohia, "Numerical analysis of Cs₂AgBiBr₆ double-perovskite solar cell with optimized performance," Nanomaterials and Energy, Vol. 12, No. 3, pp. 131–138, 2023.

[10] M. K. Hossain et al., "Combined DFT, SCAPS-1D, and wxAMPS frameworks for design optimization of efficient Cs₂AgBiBr₆-based solar cells," RSC Adv., Vol. 12, No. 34, pp. 35023–35032, 2022.

[11] M. Kibou, Z. Haman, N. Khosossi, I. Essaoudi, A. Ainane, and R. Ahl Laamara, "Computational insights into the optoelectronic potential of Cs₂AgGaBr₆ double halide perovskite solar cells," Mater. Chem. Phys., Vol. 294, Art. No. 126978, Jan. 2023.

[12] M. J. Islam, S. H. Cheragee, M. A. H. Chowdhury, S. Subrina, M. Hossain, and F. Gulshan, "Numerical Study of Higher Efficiency Perovskite Solar Cell Using Density Functional Theory," Int. Conf. on Advances in Computing, Communication, Electrical, and Smart Systems, pp. 1617–1623, 2024.

[13] K. F. Brennan, The Physics of Semiconductors: With Applications to Optoelectronic Devices, Cambridge University Press, 1999.

[14] M. J. Islam et al., "Numerical Study of Higher Efficiency Perovskite Solar Cell Using Density Functional Theory," in Proc. Int. Conf. on Advances in Computing, Communication, Electrical, and Smart Systems, pp. 1–5, 2024.

[15] M. K. Hossain et al., "Effect of Various Electron and Hole Transport Layers on the Performance of CsPbI3-Based Perovskite Solar Cells: A Numerical Investigation in DFT, SCAPS-1D, and wxAMPS Frameworks," ACS Omega, Vol. 7, No. 47, pp. 43210–43230, 2022.

[16] M. J. Islam, M. Tarek, and F. Gulshan, "A numerical analysis of a high-efficiency solar cell using a DFT explored nontoxic perovskite material," Int. Conf. Adv. Appl. Electr. Eng. Energy, pp. 1–5, 2024.

[17] M. J. Islam, S. H. Cheragee, M. A. Haque Chowdhury, S. Subrina, M. Hossain, and F. Gulshan, "Numerical study of higher efficiency perovskite solar cell using density functional theory," Int. Conf. Adv. Comput., Commun., Electr., Smart Syst. pp. 1–5, 2024.

[18] M. K. Hossain et al., "Combined DFT, SCAPS-1D, and wxAMPS frameworks for design optimization of efficient Cs2BiAgI6-based perovskite solar cells with different charge transport layers," RSC Adv., Vol. 12, No. 54, pp. 35002–35025, 2022.

[19] K. I. Ferdous Utsho et al., "Optimizing Cs2CuBiBr6 double halide perovskite for solar applications: the role of electron transport layers in SCAPS-1D simulations," RSC Adv., Vol. 15, No. 3, pp. 2184–2204, 2025.